Integration of 3D macroscopic graphene aerogel with 0D-2D AgVO$_3$-g-C$_3$N$_4$ heterojunction for highly efficient photocatalytic oxidation of nitric oxide

Dongni Liu, Dongyun Chen*, Najun Li, Qingfeng Xu, Hua Li, Jinghui He, Jianmei Lu*

Collaborative Innovation Center of Suzhou Nano Science and Technology, College of Chemistry Chemical Engineering and Materials Science Soochow University, 199 Ren'ai Road, Suzhou 215123, PR China

ARTICLE INFO

ABSTRACT

The application of three-dimensional (3D) aerogels for immobilizing powder catalysts can greatly enhance the catalyst cycling stability. In this study, we modify two-dimensional (2D) graphitic carbon nitride (g-C$_3$N$_4$) nanosheets with zero-dimensional (0D) silver metavanadate (AgVO$_3$) quantum dots. The resulting 0D-2D heterojunction facilitates the separation of electron-hole pairs, and exhibits high efficiency for removing nitric oxide (NO) at low concentrations (600 ppb) at room temperature. The removal efficiency is much higher than that of pure g-C$_3$N$_4$. The porous network framework of the 3D AgVO$_3$-g-C$_3$N$_4$-graphene hybrid aerogel is formed by bridging of graphene oxide sheets. This results in the heterojunction further enhancing electron-hole separation. The modification of g-C$_3$N$_4$ promotes the separation of photogenerated carriers in a step by step manner, and enhances their oxidation-reduction ability. The AgVO$_3$-g-C$_3$N$_4$-graphene hybrid aerogel exhibits excellent catalytic activity for NO removal (maximum of 65%). Cycling experiments verify the stability and recyclability of the aerogel.

1. Introduction

Global nitrogen oxide (NO) emission and atmospheric NO concentrations have increased rapidly in the last few decades, which has effectively saturated its environmental capacity. This has also led to regional and global environmental problems such as photochemical smog, acid rain, and ozone layer depletion [1–4]. The water solubility and reactivity of NO are poor, thus the reaction of NO with water is difficult to control. Current flue gas denitrification technology suffers from significant reducing agent requirements, secondary pollution, and complicated operation [5,6]. In contrast, photocatalytic oxidation operates under mild reaction conditions with low energy consumption [7,8]. The photocatalytic oxidation pathway is consistent with the nitrogen fixation process that has a positive effect in nature [9]. Thus, photocatalytic oxidation has been widely studied for pollutant degradation [10–12]. Many semiconductor catalysts have been applied in photocatalysis [13–15]. Among them, two-dimensional (2D) graphitic carbon nitride (g-C$_3$N$_4$) is an attractive material for the photocatalytic degradation of NO, because of its high visible light absorption and high NO degradation efficiency [16–18].

Pure semiconductor catalysts generally do not possess both narrow band gaps and high electron-hole separation abilities. g-C$_3$N$_4$ has good chemical and thermodynamic stabilities, and can be readily modified

and recycled [19]. Thus, many studies have aimed to promote photogenerated carrier migration in g-C$_3$N$_4$, using methods such as noble metal deposition [20], metal ion doping [21], non-metal doping [22], and semiconductor coupling [23]. The recent development of zero-dimensional (0D) quantum dots (QDs) has resulted in much interest from the catalysis community. QDs possess useful properties such as small size, short charge-transfer length and size-tunable optoelectronics, which can potentially be exploited in photocatalysis [24]. Cao and co-workers loaded CdS QDs into g-C$_3$N$_4$ through a solvothermal method, which increased the hydrogen evolution efficiency under visible light [25]. Chen and co-workers reported that the Bi$_2$WO$_6$ QD/g-C$_3$N$_4$ binary heterojunction greatly enhanced the photodegradation of rhodamine B [26]. Wang and co-workers constructed a Bi$_3$TaO$_7$ QD/g-C$_3$N$_4$ nanosheet 0D/2D Z-scheme composite, which could efficiently degrade antibiotics under visible light [27]. Many studies have reported the preparation of 0D-2D heterojunctions. 0D QDs can be uniformly dispersed on 2D g-C$_3$N$_4$ nanosheets, to facilitate the rapid transfer of photogenerated electrons and holes, and in turn exert their respective redox effects.

Light-weight powder catalysts exposed to air are readily blown away, which limits their ability to be subsequently recycled. Tong and co-workers prepared a g-C$_3$N$_4$/graphene oxide (GO) aerogel mixture with a macroscopic three-dimensional (3D) structure, and applied it in
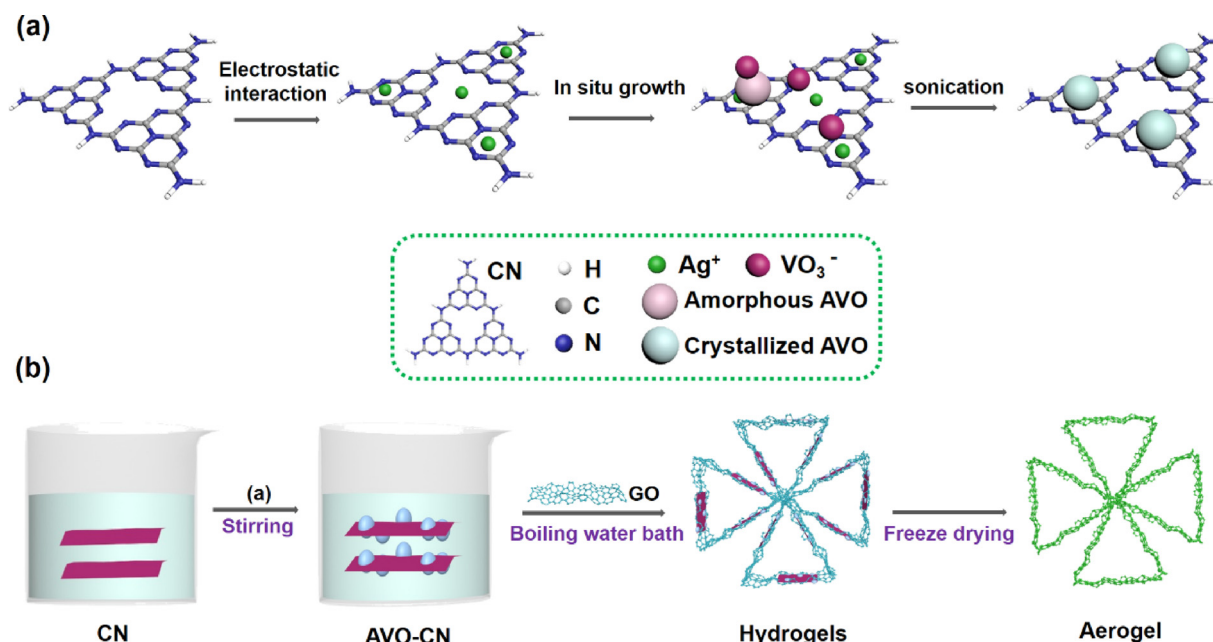
* Corresponding authors.
  E-mail addresses: dychen@suda.edu.cn (D. Chen), lujm@suda.edu.cn (J. Lu).

(a)

Electrostatic interaction

In situ growth

sonication

CN · H ● Ag⁺ ● VO₃⁻
○ H ● Amorphous AVO
● C ● Crystallized AVO
● N

(b)

(a)
Stirring

GO
Boiling water bath

Freeze drying

CN

AVO-CN

Hydrogels

Aerogel

Scheme 1. Schematic illustration of the fabrication of AVO-CN-GA composite.

visible light-induced water mediation [28]. The resulting performance was attributed to the well-defined flexible 3D architecture. The highly porous and conductive network provided abundant channels for efficient electron transfer and hole diffusion.

Based on the above studies, we designed and synthesized a 3D hybrid aerogel catalyst, shown in Scheme 1. First, $AgVO_3$ (denoted as AVO) is grown in situ on the $g-C_3N_4$ (denoted as CN) in a two-step process. Specifically, the N sites of CN combine with Ag^+ via electrostatic interaction. The Ag^+ then forms AVO with VO_3^-, and then forms a 0D-2D $AgVO_3-g-C_3N_4$ (denoted as AVO-CN) heterojunction through the formation of C=O bonds. Second, AVO-CN and GO form a hydrogel in a boiling water bath. Subsequent freeze-drying yields the target catalyst $AgVO_3-g-C_3N_4$-graphene aerogel (denoted as AVO-CN-GA). The robust heterojunction within the 0D-2D AVO-CN catalyst inhibits the recombination of photogenerated electrons and holes. Introducing GO further enhances the separation of photogenerated carriers, and provides the catalyst with a macroscopic, light-weight sponge-like morphology. This layer-by-layer design is conducive to photocatalytic oxidation-reduction. The 2D CN nanosheets and GO sheets are tightly bound by electrostatic, π-π stacking, and hydrogen-bonding interactions [29]. The photocatalytic results demonstrate that the catalyst has high efficiency (65%) for degrading NO, and has high stability over multiple reaction cycles.

2. Experimental section

2.1. Materials and reagents

All materials and reagents were used directly without further purification. Absolute ethanol and ammonia water (25 wt. %) were of analytical grade and purchased from Sinopharm Chemical Reagent Co. Ltd. (China). Dicyandiamide ($C_2H_4N_4$), graphite power (purity > 99.7%), potassium permanganate, L-ascorbic acid, metavanadate amine (NH_4VO_3) and silver nitrate ($AgNO_3$) were bought from Sigma-Aldrich. The water used in the experiments was obtained from the Millipore system (18.2 MΩ cm).

2.2. Preparation of CN and GO

The bulk CN and CN nanosheets were prepared by thermal

polycondensation of dicyandiamide in the tube furnace and air stripping oxidation in the muffle furnace with a heating rate of 5 °C/min, respectively [30]. Synthesis of GO is used the modified Hummer's method according to the previous literature [31].

2.3. Preparation of AVO-CN

Silver metavanadate quantum dots were modified onto carbon nitride by dropwise addition [32]. In a typical experiment, 20 ml $AgNO_3$ (0.0170 g, 0.1 mmol) solution was completely dissolved with a beaker wrapped in aluminum foil, then the CN (0.0243 g) were added to the above solution and stirred for one hour and the obtained suspension were subsequently sonicated for one hour. 20 ml NH_4VO_3 solution (0.0117 g, 0.1 mmol) were dispensed into the suspension via a disposable syringe (20 ml) at a rate of 60 ml/h. After that, the pH of the suspension is adjusted to neutral and sonicated for one hour. The suspension were placed in a round bottom flask in an oil bath at 80 °C for 6 h. Finally, the resulting dispersion was washed three times with ultrapure water and absolute ethanol, respectively. The product was placed in an oven at 80 °C for 8 h, resulting in the nanocomposite AVO-CN with light-yellow color. The synthesis of AVO followed the above method without addition of CN. Other nanocomposite of different silver metavanadate loadings were also synthesized via the above steps.

2.4. Preparation of AVO-CN-GA

AVO-CN-GA was formed by a simple boiling water bath [33]. The steps are as follows: 15 mg of GO was added to a glass bottle (20 ml) and 4 ml water is added in it to make GO evenly dispersed. Then 45 mg of AVO-CN was added to the GO dispersion. After ultrasonic mixing, 30 mg L-ascorbic acid was added and the mixture was placed in a boiling water bath to heat it. After half an hour, a hydrogel was formed and immediately frozen in a −40 °C freezer for 40 min. After being naturally thawed, it was put into a boiling water bath for 8 h and finally placed in a freeze dryer for two days to obtain regular shape of light-weight aerogels. Other aerogels with different heterojunction contents were obtained by adjusting the mass of GO.

2.5. Characterization

The morphologies and structures of the catalysts were characterized by Scanning electron microscopy (SEM, Hitachi S-4700) and Transmission electron microscopy (TEM, Tecnai G200). The elemental distribution and lattice spacing of the prepared samples were measured by X-ray energy dispersive spectroscopy (EDS) and high-resolution transmission electron microscopy (HRTEM, Tecnai G2 F20 S-TWIN). X-ray diffraction (XRD, X' Pert-Pro MPD) was used to analyze the crystal phase of the products. X-ray photoelectron spectroscopy (XPS) spectra and valence band edges are obtained by X-ray photoelectron spectrometer (ESCALAB MK II) with Al-Kα radiation. UV–vis spectrophotometer (CARY50) and Fourier transform infrared (FTIR) spectrometers (Nicolet 4700) were used to determine the light absorption spectra of the samples. Fluorescence spectrophotometer (FLS920) with an excitation wavelength of 395 nm was used to record the photoluminescence (PL) spectra of the products. Electrochemical impedance spectroscopy (EIS) and photocurrent were performed on CHI 660B electrochemical system (Shanghai, China). Photocatalytic mechanism was study by utilizing paramagnetic species spin-trapped with 5,5-dimethyl-l-pyrroline-*N*-oxide (DMPO) on Bruker A300EPR spectrometer to obtain the Electron spin resonance (ESR) spectra.

2.6. Photocatalytic activity evaluation

Photocatalytic measurements were used to evaluate the NO removal efficiency of the catalyst prepared under visible light irradiation at room temperature. Typically, 0.1 g of powder catalysts or aerogels were fixed to a center cardboard of in a glass cylinder container with a volume of 2.26 l ($\pi R^2 H = \pi \times 6^2 cm^2 \times 20$ cm). NO in the compressed gas bottle (10 ppm, N_2 balance) and the air in the compressed air bottle were premixed in a three-way valve and flowed through a cylindrical vessel at a flow rate of 1.2 l/min to adjust the initial concentration of NO to 600 ppb. A 300 W commercial xenon lamp was placed vertically above the reactor. When the gas reached the adsorption-desorption equilibrium on the catalyst surface (~ 0.5 h), the xenon lamp was turned on immediately. The concentration of NO was monitored every minute by a NOx analyzer (Thermo Environmental Instruments, Inc., 42i-TL). A total of 30 sets of data were measured. The NO removal efficiency was calculated by this formula: $\eta = (1-C/C_0) \times 100\%$, where C and C_0 are the outlet and feed port concentrations, respectively. The cycle test is also implemented by the above method.

2.7. Trapping experiments of active species

We use potassium iodide (KI), potassium dichromate ($K_2Cr_2O_7$), tert-butanol (TBA) and p-benzoquinone (PBQ) as scavengers for holes, electrons, hydroxyl radicals and superoxide radicals, respectively. Typically, 100 mg of catalyst and 2 mmol of capture agent were dispersed in 20 ml of water and sonicated until the suspension was evenly dispersed. It was applied to a glass dish and dried in an oven at 60 °C. Subsequent NO removal experiments were performed after drying was completed.

3. Results and discussion

3.1. XRD analysis

The crystal structures and phase compositions of CN, AVO-CN, GA, and AVO-CN-GA were characterized by X-ray diffraction (XRD) (Fig. 1). For AVO, all XRD peaks match those in the standard card of monoclinic AVO (JCPDS No. 29-1154). The XRD pattern of CN contains peaks at 12.9° and 27.8° 2θ. The weak peak (100) is due to the in-planar period, while the strong peak (002) corresponds to the stacking of planes [34]. All characteristic peaks of AVO and CN are observed in the XRD pattern of AVO-CN. In addition, a weak diffraction peak at 22.6° 2θ is observed
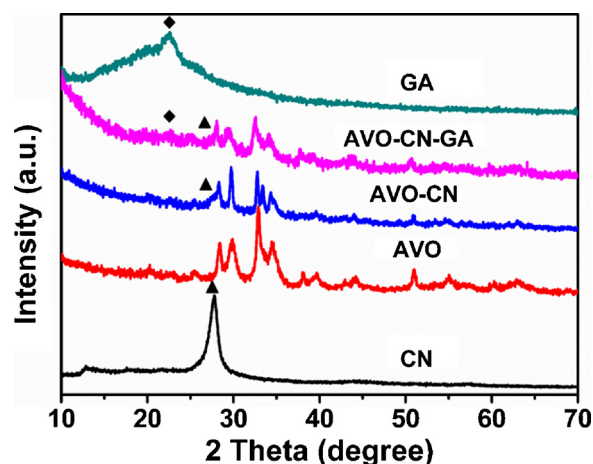

Fig. 1. XRD patterns of CN, AVO, 30 AVO-CN, 30 AVO-CN-GA-75, and GA.

in the XRD pattern of 30 AVO-CN-GA-75, which originates from the 3D bridging of reduced GO sheets [35]. This suggests the stable bonding of the nanocomposite with the 3D aerogel.

3.2. Morphology and structure

Scanning electron microscopy (SEM) and transmission electron microscopy (TEM) were used to characterize the morphology and structure of CN, AVO, and AVO-CN-GA containing different mass loadings of AVO-CN. TEM and SEM images show the ultrathin sheets and irregular wrinkles of CN (Fig. 2a and S1). The AVO QDs are evenly dispersed on the CN by the in situ growth method (Fig. 2b). Statistical analysis indicates that the average diameter of the loaded AVO is about 3.5 nm (Fig. 2c). The HRTEM image shows that the lattice spacing of AVO is 0.389 nm, which is consistent with the (-202) facet of monoclinic AgVO$_3$ (Fig. 2**d**) [32]. The selected area electron diffraction pattern shows the polycrystalline nature of the AVO QDs (Fig. S2). AVO with different mass loadings (Fig. S3a-d) were also prepared to investigate the effect of loading on photocatalytic performance. In this series of catalysts, an AVO loading of 30 wt.% (denoted as 30 AVO-CN) results in well-dispersed AVO with no agglomeration. The TEM images (Fig. 2**e, f**) show that AVO-CN can be readily combined with GO (Fig. 3). This conclusion is supported by the SEM image shown inset in Fig. 3**b**. A digital photograph of the macro hybrid aerogel is shown in the upper right corner of Fig. 3a, and we can obtain porous structures as shown in Figs. 3**a, b** by taking a small piece of the aerogel. In other words, the layer stack of these porous structures forms a macroscopic layered porous hybrid aerogel. The layered porous structure has two advantages: one is that the porous structures facilitate the smooth circulation of NO; the other is that the layered structure ensures that the gas molecules are trapped in the layer during the circulation process, and can fully contact the active material AVO-CN on the GO surface to achieve the goal of fully degrading NO. Energy-dispersive spectroscopy (EDS) mapping images (Fig. S4) show the existence of C and N in CN, Ag, O, and V in AVO, and C and O in GO. The SEM-EDS spectrogram (Fig. S5) shows the ratio of the elements in each sample.

3.3. XPS analysis

X-ray photoelectron spectroscopy (XPS) spectra of the C 1 s, N 1 s, O 1 s, V 2p, and Ag 3d regions for 30 AVO-CN-GA-75 (30 AVO-CN is 75 wt.%) are shown in Fig. 4. The carbon peak at 284.8 eV originates from C−C and C═C bonds in CN and GO [28], and also from surface carbon bound to oxygen in air. The peak at 285.9 eV is attributed to sp^2-hybridized C bound to N within the aromatic structure. The higher energy peak at 288.6 eV is assigned to sp^2-hybridized C in aromatic rings attached to
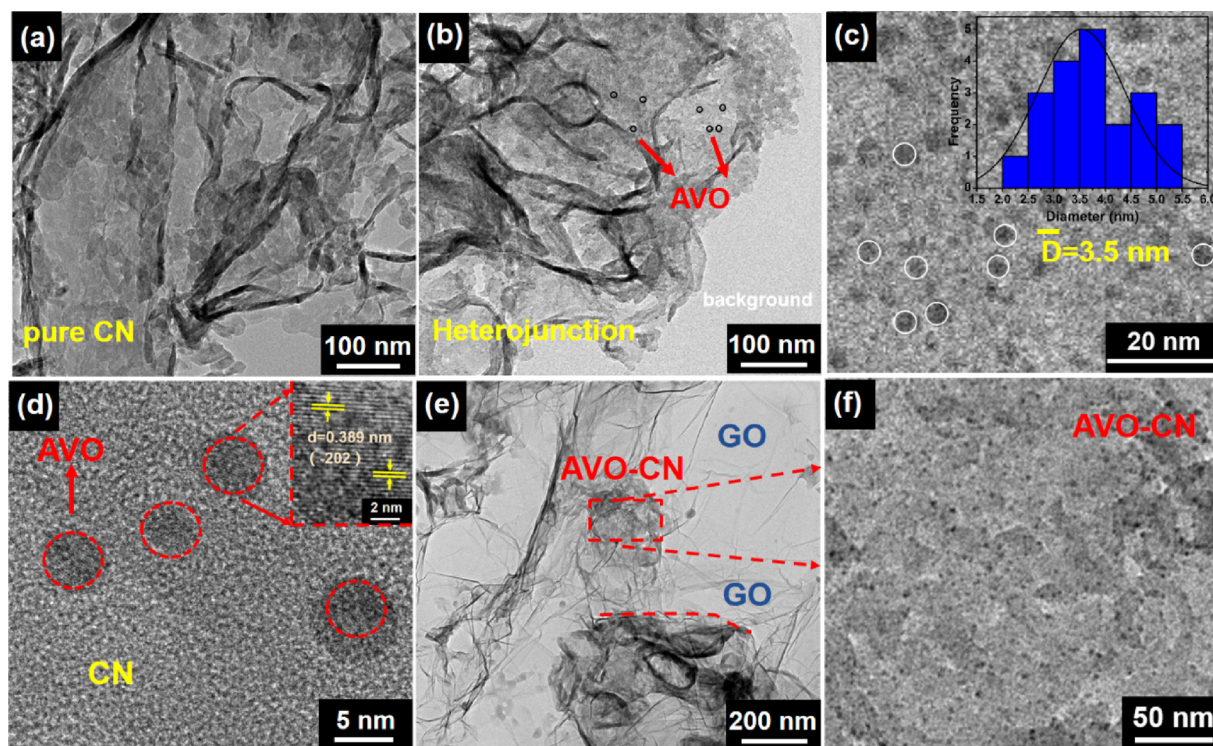
Fig. 2. TEM images of (a) CN, (b) 30 AVO-CN, and (c) 30 AVO-CN. (d) HRTEM image of 30 AVO-CN. TEM image of (e) 30 AVO-CN-GA-75, and TEM image of (f) 30 AVO-CN in high magnification corresponding to the marked area in (e). The size distribution histogram for AVO (sample count of 20) is shown inset in (c).

NH_2 groups [36]. Peaks in the N 1 s spectrum at 398.5 eV and 400.8 eV are consistent with these two binding states. Peaks at 286.9 eV and 288.1 eV in the C 1 s spectrum are characteristic of GO, and their presence indicates the combination of AVO-CN and GO. The new broad peak at 292.2 eV in the C 1 s spectrum is due to the strong binding of the 0D/2D heterojunction, i.e., O in AVO forms C=O bonds with C in CN [27]. The corresponding C=O peak of the heterojunction occurs at 533.5 eV in the O 1 s spectrum. The remaining O 1 s peak can be deconvoluted into three peaks at 530.0 eV, 531.1 eV, and 532.0 eV, which are attributed to the binding energies of V=O, C–O, and V–O, respectively. Peaks at 516.8 eV and 524.4 eV in the V 2p spectrum correspond to the V $2p_{3/2}$ and V $2p_{1/2}$ states, respectively [37]. The Ag 3d spectrum contains two strong peaks at 368.1 eV and 374.0 eV, which are assigned to the Ag $3d_{5/2}$ and Ag $3d_{3/2}$ states, respectively [37]. In summary, the XPS spectra for the elements demonstrate the strong linkage within the 3D AVO-CN-GA composite.

Fourier-transform infrared (FT-IR) spectra also demonstrate the formation of the 0D-2D heterojunction and its combination with GO (Fig. 5d). The FT-IR spectrum of CN contains a sharp absorption peak at

809 cm^{-1}, which is attributed to the stretching vibration modes of s-triazine ring units [38]. A series of peaks at 1233–1637 cm^{-1} is attributed to the vibration of C–N bonds in carbon-nitrogen heterocycles, while the absorption peak centered at 3182 cm^{-1} is attributed to the N–H bond [38]. The C–N absorption peak at 809 cm^{-1} blueshifts to 801 cm^{-1} after loading of the AVO QDs. The peaks of the N–H stretching vibrations and CN heterocycle stretching vibrations in the spectrum of 30 AVO-CN are of much lower intensity. During synthesis, Ag^+ is adsorbed at the N sites of CN, which disrupts N–H bonds and impedes the vibrations of the C–N heterocycle. All peaks associated with bonds of 30 AVO-CN and GA are present in the FT-IR spectrum of 30 AVO-CN-GA-75. This indicates that the structures of graphene and the heterojunction are maintained after freeze-drying. FT-IR peaks of AVO-CN and 30 AVO-CN-GA with different loadings are shown in Fig. S6. For AVO-CN, as the AVO loading increases, the stretching vibrations of the C–N heterocyclic ring and C–H bond weaken. The intensity of the absorption peaks of AVO-CN decrease upon the addition of GO sheets. This is mainly attributed to the reduced mass of the 0D-2D heterojunction.
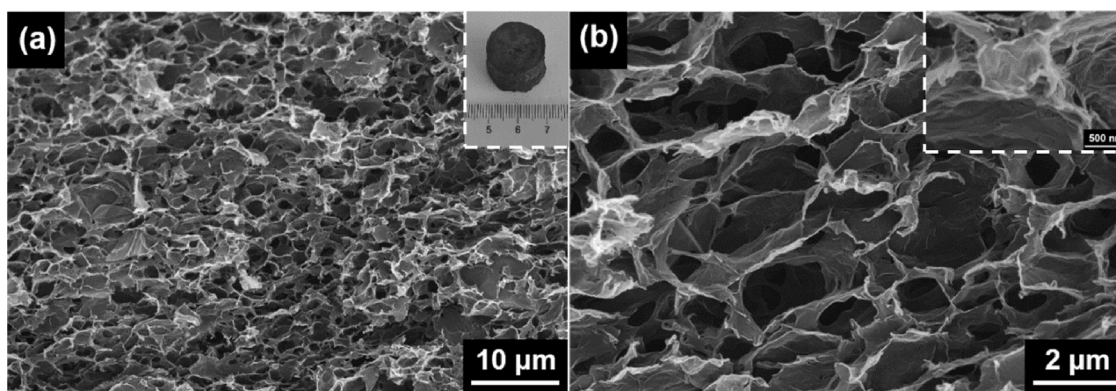

Fig. 3. SEM images of 30 AVO-CN-GA-75. A digital photograph of the sample is shown inset in (a).
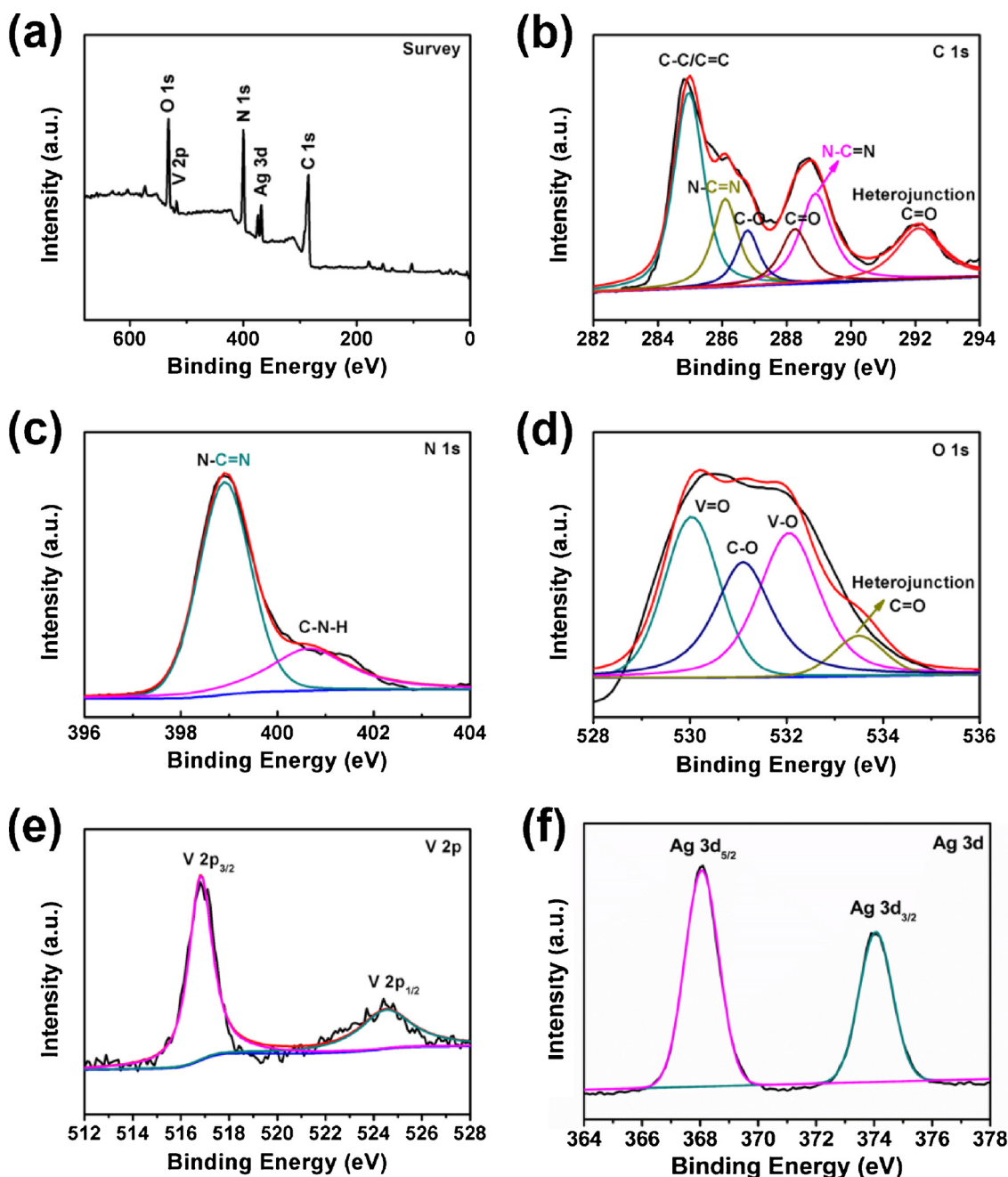
Fig. 4. (a) XPS survey scan and high-resolution (b) C 1 s, (c) N 1 s, (d) O 1 s, (e) V 2p, and (f) Ag 3d spectra of 30 AVO-CN-GA-75.

3.4. Optical properties

Ultraviolet-visible (UV–vis) diffuse reflectance spectra (DRS) of the samples are shown in Fig. 5a. The maximum absorption edges of CN containing different QD loadings are red-shifted with increasing QD loading, and the absorption of visible light simultaneously improves. After incorporating GO, the hybrid aerogels exhibit similar absorption edges to that of 30 AVO-CN. This indicates that forming the hybrid aerogel does not diminish the absorption of visible light. Fig. 5b shows the optical band gaps of CN and AVO, which are 2.89 eV and 2.55 eV, respectively. Combining the band gap information with the XPS valence bands (Fig. S7) gives information about the conduction band edges of the catalysts. This in turn can be used to elucidate the photocatalytic mechanism.

Photoluminescence (PL) spectra were recorded to investigate the separation efficiency of photogenerated electrons and holes (Fig. 5c).

The PL spectrum of CN has an emission peak maximum at 486 nm at an excitation wavelength of 395 nm. Increasing the AVO QD loading in the composite causes the emission peak maximum to redshift, which is consistent with the results for the UV absorption edge. The decrease in fluorescence intensity with increasing QD loading indicates the improved separation of electron-hole pairs. Subsequent introduction of the three-dimensional graphene network enhances the conductivity of the system. This suppresses carrier recombination, and the fluorescence intensity follows the trend: 30 AVO-CN-GA-75 < 30 AVO-CN-GA-50 < 30 AVO-CN-GA-90. The modified aerogel exhibits weaker fluorescence, so is potentially a good photocatalyst.

3.5. Electrochemical properties

Electrochemical impedance spectroscopy (EIS) was used to investigate the carrier separation, electron transfer efficiency, and
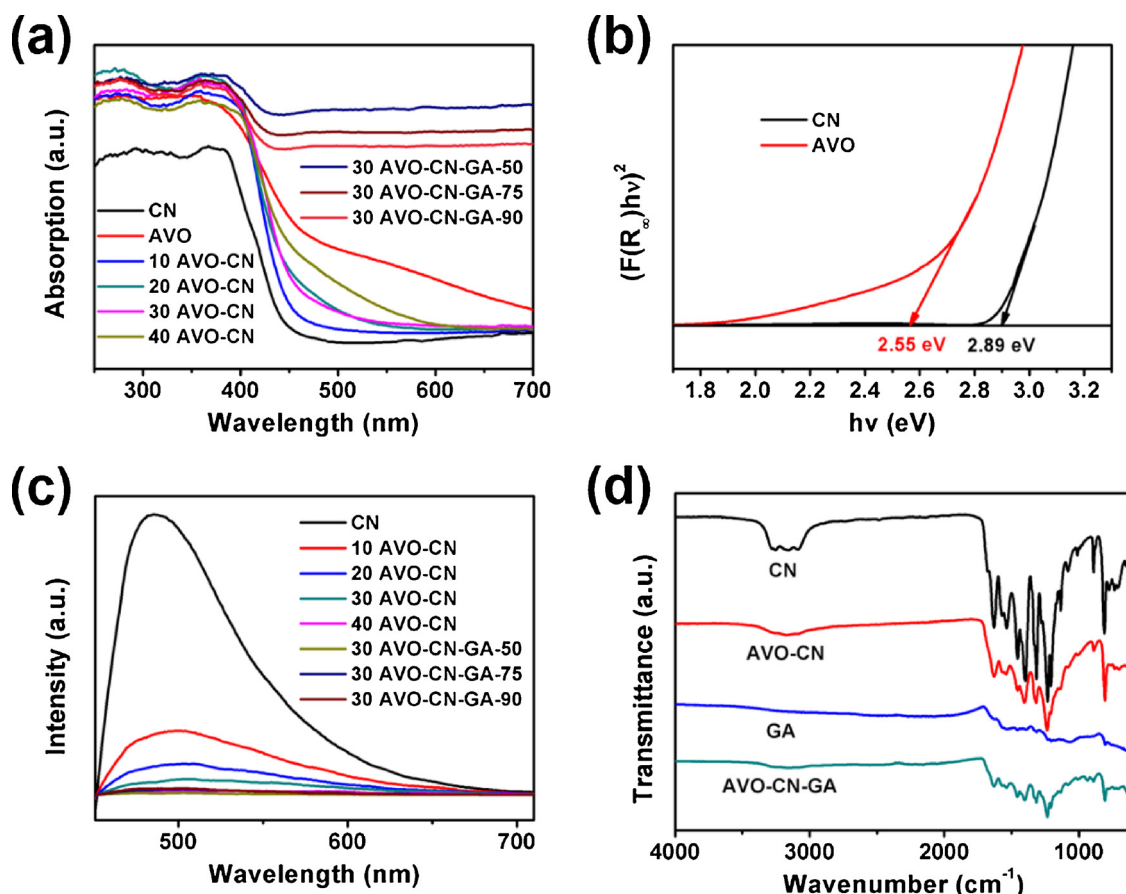
Fig. 5. (a) UV–vis DRS spectra, (b) Plots of $(F(R_\infty)h\nu)^2$ versus $h\nu$ for estimating the optical band gaps, (c) PL spectra obtained following excitation at 395 nm, and (d) FT-IR spectra of the samples.

interfacial charge transfer of electron-hole pairs after surface modification and combination with GO. Fig. 6a shows that the Nyquist plots are semicircles with subsequent straight lines with slopes of 45°. The charge transfer resistance of AVO-CN is the smallest when the QD loading is 30 wt.%. The charge removal efficiency is the highest when the content of 30 AVO-CN is 75 wt.% in 30 AVO-CN-GA. In addition, the photocurrent density response test (Fig. S8) shows the following order: CN < 30 AVO-CN < 30 AVO-CN-GA-75, supporting the above impedance information. These illustrate that the addition of GO enhances the overall conductivity of the catalyst.

3.6. Photocatalytic performance and stability

Photocatalytic degradation tests of NO were carried in a laboratory environment to evaluate the catalytic performances of CN, AVO-CN, and AVO-CN-GA. Fig. 6 shows the relationship between C/C_0 and degradation time, where C and C_0 are the outlet and feed port concentrations, respectively. The NO degradation efficiency of CN is 32% (Fig. 6b), which is consistent with our previous studies [39,40]. The degradation efficiency of AVO QDs is unsatisfactory, despite its wide visible absorption width. Electron-hole pairs in the composite are satisfactorily transferred and separated, due to the formation of the AVO-CN heterojunction. Increasing the AVO loading enhances NO degradation. When the loading is 30 wt.%, 55% of NO is degraded. The corresponding cycling degradation test demonstrates the stability of the catalyst (Fig. S9). The NO degradation efficiency of 40 AVO-CN-CN is much lower than those of the other samples. TEM images (Fig. S3c, d) show the 40 AVO-CN contains many agglomerated and free AVO QDs. As mentioned above, pure AVO QDs exhibit almost no degradation of NO. Thus, 30 AVO-CN and GO were used to prepare a series of aerogels.

When the proportion of 30 AVO-CN is 75 wt.%, the degradation efficiency is improved by 10% (Fig. 6c). Compared with the other photocatalysts used to degrade NO, the degradation efficiency was greatly improved (Table 1). This is attributed to the strong charge separation ability of GO. The 3D porous structure promotes the transport of NO gas molecules to the active sites AVO-CN, which promotes catalysis. The degradation effect of pure GA is shown in Fig. S10.The photocatalytic efficiencies of 30 AVO-CN-GA-50 and 30 AVO-CN-90 are not optimized due to their low heterojunction contents, so they do not completely inhibit electron-hole recombination.

Catalyst stability is an important environmental consideration. Five consecutive NO degradation cycles were carried out using 30 AVO-CN-GA-75 (Fig. 6d). The aerogel retains its regular morphology, and the degradation efficiency decreases by 6% over these five cycles. These results demonstrate the good cycling performance and stability of the photocatalyst. In addition, XPS spectra (Fig. S11) show that Ag^+ in AVO was reduced to a small amount of metallic silver ($Ag°$) under light conditions [45], but the degradation effect of the system was only slightly decreased (Figs. 6d and S9).

3.7. Photocatalytic mechanism for NO removal

Electron spin resonance tests were carried out using 5,5-dimethyl-1-pyrroline-*N*-oxide (DMPO) to detect superoxide radicals ($^\cdot O_2^-$) and hydroxyl radicals ($^\cdot OH$) generated by 30 AVO-CN-GA-75 under visible light irradiation. Fig. 7a shows the four uniform sized peaks of DMPO-$^\cdot O_2^-$ after irradiation for 2 min. The four peaks of DMPO- $^\cdot OH$ are also observed under visible light irradiation, and their intensity ratio is 1:2:2:1 (Fig. 7b) [46]. These two radicals and photogenerated holes (h^+) and e^- are the active species in the NO degradation process.
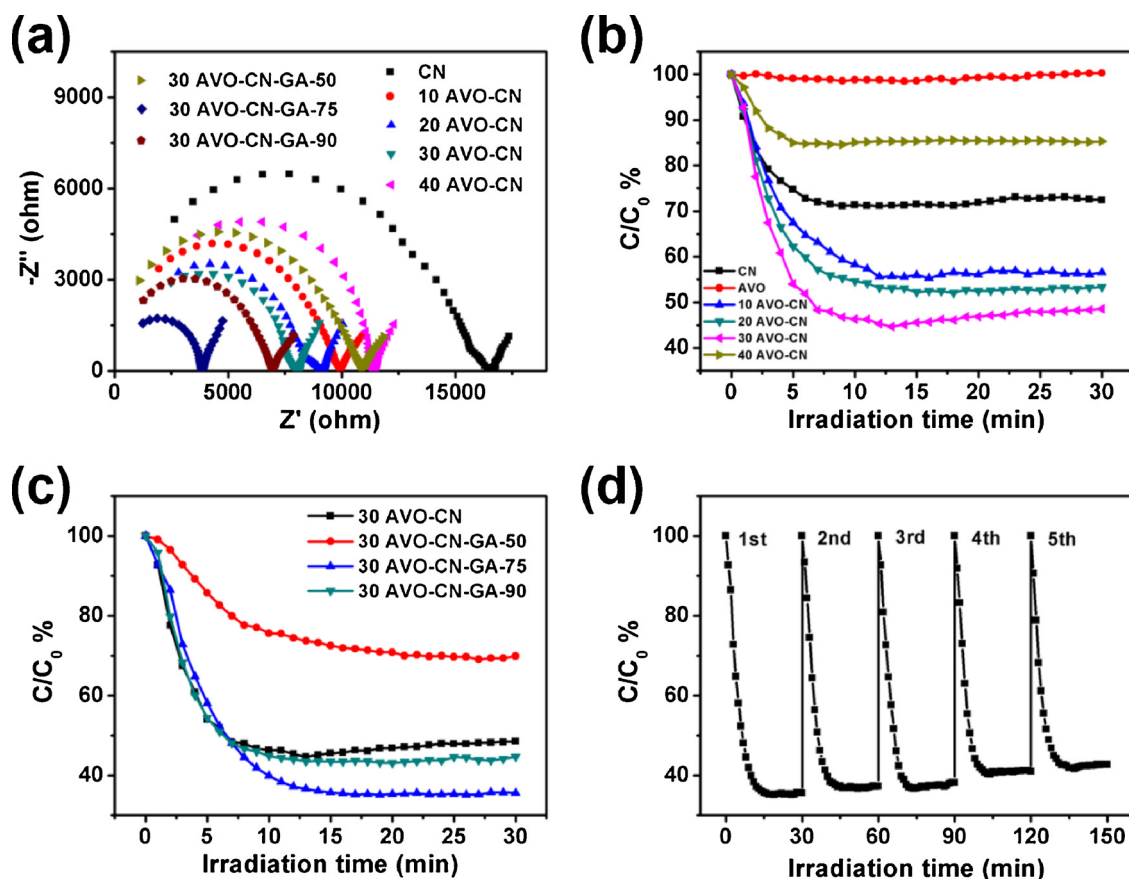
Fig. 6. (a) EIS spectra of samples under visible light irradiation, (b, c) photocatalytic activities of samples for NO removal under visible light irradiation, and (d) five consecutive photocatalytic reaction cycles over 30 AVO-CN-GA-75.

Table 1
Comparison of efficiency of removing NO by different catalysts.

Catalyst	catalyst (mg)	NO (ppb)	light type	degradation time (min)	$\eta_{(NO)}$ (%)	ref.
$Bi_2O_2CO_3$-g-C_3N_4	100	400	Xe-lamp 300w	30	35	[41]
BiOBr-graphene	100	400	Xe-lamp 300w	30	40	[42]
CQDs-FeOOH	100	400	Xe-lamp 300w	30	34	[43]
$Bi_2Sn_2O_7$	200	400	Xe-lamp 300w	60	37	[44]
$Pb_2BiTi_5O_{18}$	50	500	Xe-lamp 300w	25	50	[18]
PI-g-C_3N_4	50	600	Xe-lamp 300w	50	47	[16]
CN-OLa	100	500	Xe-lamp 150w	30	50.4	[52]
Bi@BiOSi	200	450	Xe-lamp 150w	30	50.2	[53]
O-ACN-Ba	200	500	Xe-lamp 150w	30	56.4	[54]
AVO-CN-GA	100	600	Xe-lamp 300w	30	65	this work

To further explore the role of active free radicals in photocatalytic processes, we conducted a series of capture experiments on 30 AVO-CN (Fig. S13) [16]. The results show that photogenerated electrons and holes are critical in the degradation process of NO. The addition of PBQ trapping agent significantly reduced the degradation efficiency of NO, indicating the important contribution of $\cdot O_2^-$ in the photocatalytic process. In addition, the experimental results also show that $\cdot OH$ is a minor active free radical, but it also plays a non-negligible role in catalyzing NO. The valence band edges and conduction band edges derived from the XPS valance spectra (Fig. S7) can be used to deduce a photocatalytic mechanism for the system (Fig. 8). GO promotes the transfer of electrons, enhances the overall electrical conductivity, and improves the photocatalytic efficiency. CN and AVO generate electron-hole pairs under visible light irradiation, as shown in equation (1). The positions of the band edges suggest that photogenerated electrons in CN transfer to the conduction band of AVO, and holes in AVO

simultaneously transfer to the valence band (VB) of CN. This process is consistent with that expected for a type-II heterojunction [47]. The charge separation promotes photocatalysis. Due to the relative positive VB potential of CN (2.03 eV vs NHE) to NO_3^-/NO (0.94 eV vs NHE), holes on VB of CN can directly oxidize NO to NO_3^- in the presence of water in the air [40,41,48], as shown in equation (2). $\cdot O_2^-$ is the main active species in the photocatalytic degradation of NO, and is produced by the reduction of O_2 in air, as shown in equation (3). $\cdot O_2^-$ then oxidizes NO, as shown in equation (4). The photogenerated electrons could also reduce O_2 to H_2O_2 due to the redox potential of O_2/H_2O_2 (0.695 eV vs NHE), and afterward, the formed H_2O_2 would be further transformed into $\cdot OH$ by trapping an electron, as shown in equation (5)–(6) [46,49,50]. NO_3^- is obtained after the two-step reaction, as shown in equations (7)–(8). The amount of NO_2 produced during photodegradation was also detected (Fig. S12) [51], and compared with CN, 30 AVO-CN-GA-75 produced less amount of NO_2, which facilitated
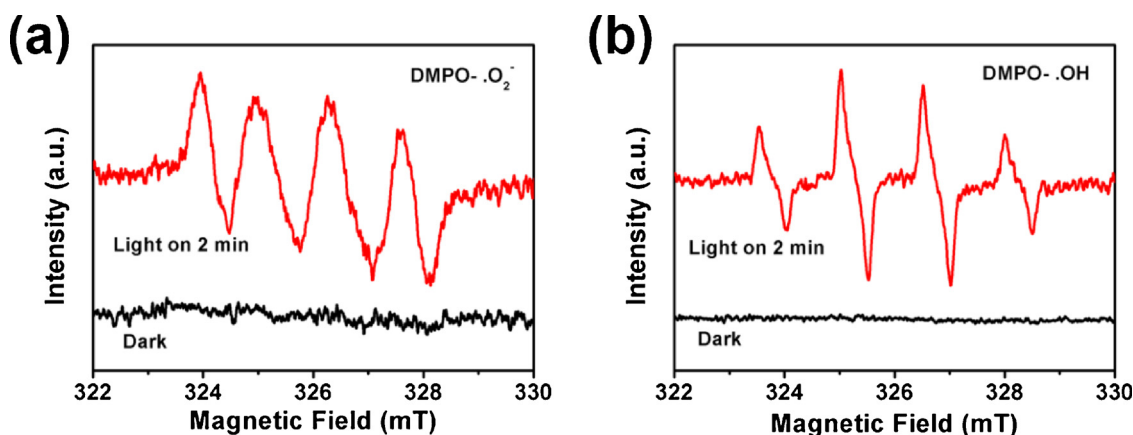
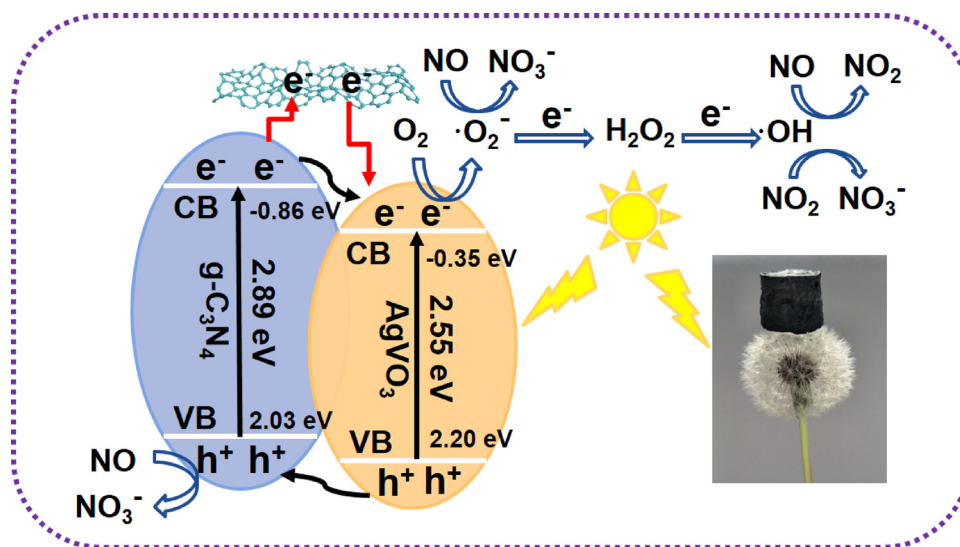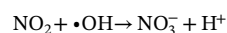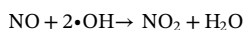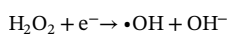**Fig. 7.** (a) DMPO- $\cdot O_2^-$ and (b) DMPO- $\cdot$OH profiles for 30 AVO-CN-GA-75.
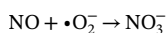

Fig. 8. Mechanism for the photocatalytic removal of NO.

the smooth progress of the photocatalysis.

$$AVO\text{-}CN/AVO\text{-}CN\text{-}GA + h\nu \rightarrow e^- + h^+ \tag{1}$$

$$NO + 2H_2O + 3h^+ \rightarrow NO_3^- + 4H^+ \tag{2}$$

$$O_2 + e^- \rightarrow \cdot O_2^- \tag{3}$$

$$NO + \cdot O_2^- \rightarrow NO_3^- \tag{4}$$

$$\cdot O_2^- + 2H^+ + e^- \rightarrow H_2O_2 \tag{5}$$

$$H_2O_2 + e^- \rightarrow \cdot OH + OH^- \tag{6}$$

$$NO + 2\cdot OH \rightarrow NO_2 + H_2O \tag{7}$$

$$NO_2 + \cdot OH \rightarrow NO_3^- + H^+ \tag{8}$$
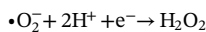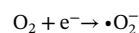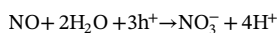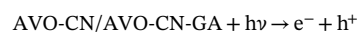
4. Conclusions

The 3D porous aerogel AVO-CN-GA was prepared for degrading NO at the ppb level under visible light irradiation. The construction of the heterojunction improved the separation of electron-hole pairs, which resulted in a maximum NO degradation ratio of 65%. Introducing GO enhanced the conductivity, visible light adsorption, recyclability, and stability of the photocatalyst. Cycling tests demonstrated the stability and potential commercial application of the system.

Appendix A. Supplementary data

Supplementary material related to this article can be found, in the online version, at doi:https://doi.org/10.1016/j.apcatb.2018.11.012.

References

[1] X. Liu, Z. Fu, B. Zhang, L. Zhai, M. Meng, J. Lin, J. Zhuang, G.G. Wang, J. Zhang, Effects of sulfuric, nitric, and mixed acid rain on Chinese fir sapling growth in Southern China, Ecotox. Environ. Saf. 160 (2018) 154–161.
[2] T. Jurkat, C. Voigt, S. Kaufmann, J.U. Grooß, H. Ziereis, A. Dörnbrack, P. Hoor, H. Bozem, A. Engel, H. Bönisch, Depletion of ozone and reservoir species of chlorine and nitrogen oxide in the lower Antarctic polar vortex measured from aircraft, Geophys. Res. Lett. 44 (2017) 6440–6449.
[3] E.S. Cramer, M.S. Briggs, N. Liu, B. Mailyan, J.R. Dwyer, H.K. Rassoul, The impact

on the ozone layer from NO$_x$ produced by terrestrial gamma ray flashes, Geophys. Res. Lett. 44 (2017) 5240–5245.

[4] R.S. Stolarski, A.R. Douglass, L.D. Oman, D.W. Waugh, Impact of future nitrous oxide and carbon dioxide emissions on the stratospheric ozone layer, Environ. Res. Lett. 10 (2015) 034011.

[5] F. He, X. Deng, M. Chen, Evaluation of Fe(II)EDTA-NO reduction by zinc powder in wet flue gas denitrification technology with Fe(II)EDTA, Fuel 199 (2017) 523–531.

[6] H.T. Karlsson, H.S. Rosenberg, Flue gas denitrification. Selective catalytic oxidation of nitric oxide to nitrous oxide, Ind. Eng. Chem. Process Des. Dev. 23 (1984) 808–814.

[7] D. Sun, Y. Lin, Z. Li, Visible-light-assisted aerobic photocatalytic oxidation of amines to imines over NH$_2$-MIL-125(Ti), Appl. Catal. B 164 (2015) 428–432.

[8] P. Niu, L. Zhang, G. Liu, H.M. Cheng, Graphene-like carbon nitride nanosheets for improved photocatalytic activities, Adv. Funct. Mater. 22 (2012) 4763–4770.

[9] H. Li, J. Shang, Z. Ai, L. Zhang, Efficient visible light nitrogen fixation with BiOBr nanosheets of oxygen vacancies on the exposed {001} facets, J. Am. Chem. Soc. 137 (2015) 6393–6399.

[10] S.C. Yan, Z.S. Li, Z.G. Zou, Photodegradation performance of g-C$_3$N$_4$ fabricated by directly heating melamine, Langmuir 25 (2009) 10397–10401.

[11] H. Wei, W.A. Mcmaster, J.Z.Y. Tan, D. Chen, R.A. Caruso, Tricomponent brookite/anatase TiO$_2$/g-C$_3$N$_4$ heterojunction in mesoporous hollow microspheres for enhanced visible-light photocatalysis, J. Mater. Chem. A Mater. Energy Sustain. 6 (2018) 7236–7245.

[12] H. Zangeneh, A.A.L. Zinatizadeh, M. Habibi, M. Akia, M.H. Isa, Photocatalytic oxidation of organic dyes and pollutants in wastewater using different modified titanium dioxides: a comparative review, J. Ind. Eng. Chem. 26 (2015) 1–36.

[13] Y. Xie, S. Yu, Y. Zhong, Q. Zhang, Y. Zhou, SnO$_2$/Graphene quantum dots composited photocatalyst for efficient nitric oxide oxidation under visible light, Appl. Surf. Sci. 448 (2018) 655–661.

[14] L. Yang, Y. Liu, R. Zhang, W. Li, P. Li, X. Wang, Y. Zhou, Enhanced visible-light photocatalytic performance of a monolithic tungsten oxide/graphene oxide aerogel for nitric oxide oxidation, Chin. J. Catal. 39 (2018) 646–653.

[15] J. Ran, G. Gao, F.T. Li, T.Y. Ma, A. Du, S.Z. Qiao, Ti$_3$C$_2$ MXene co-catalyst on metal sulfide photo-absorbers for enhanced visible-light photocatalytic hydrogen production, Nat. Commun. 8 (2017) 13907.

[16] G. Dong, L. Yang, F. Wang, L. Zang, C. Wang, Removal of nitric oxide through visible light photocatalysis by g-C$_3$N$_4$ modified with perylene imides, ACS Catal. 6 (2016) 6511–6519.

[17] J. Hu, D. Chen, N. Li, Q. Xu, H. Li, J. He, J. Lu, In Situ Fabrication of Bi$_2$O$_2$CO$_3$/MoS$_2$ on carbon nanofibers for efficient photocatalytic removal of NO under visible-light irradiation, Appl. Catal. B 217 (2017) 224–231.

[18] R. Hailili, G. Dong, Y. Ma, S. Jin, C. Wang, T. Xu, Layered perovskite Pb$_2$Bi$_4$Ti$_5$O$_{18}$ for excellent visible light-driven photocatalytic NO removal, Ind. Eng. Chem. Res. 56 (2017) 2908–2916.

[19] A. Vinu, Two-dimensional hexagonally-ordered mesoporous carbon nitrides with tunable pore diameter, surface area and nitrogen content, Adv. Funct. Mater. 18 (2008) 816–827.

[20] X. Liu, P. Su, Y. Chen, B. Zhu, S. Zhang, W. Huang, g-C$_3$N$_4$ supported metal (Pd, Ag, Pt) catalysts for hydrogen-production from formic acid, New J. Chem. 42 (2018) 9449–9454.

[21] W. Niu, K. Marcus, L. Zhou, Z. Li, L. Shi, K. Liang, Y. Yang, Enhancing electron transfer and electrocatalytic activity on crystalline carbon-conjugated g-C$_3$N$_4$, ACS Catal. 8 (2018) 1926–1931.

[22] Y.P. Zhu, T.Z. Ren, Z.Y. Yuan, Mesoporous phosphorus-doped g-C$_3$N$_4$ nanostructured flowers with superior photocatalytic hydrogen evolution performance, ACS Appl. Mater. Interfaces 7 (2015) 16850–16856.

[23] Z. Zhao, Y. Sun, F. Dong, Graphitic carbon nitride based nanocomposites: a review, Nanoscale 7 (2014) 15–37.

[24] G.H. Carey, A.L. Abdelhady, Z. Ning, S.M. Thon, O.M. Bakr, E.H. Sargent, Colloidal quantum dot solar cells, Chem. Rev. 115 (2015) 12732–12763.

[25] Shao-Wen Cao, Jun Fang, M. Mehdi Shahjamali, Y.C. Freddy Boey, S.C. Joachim Loo, In-situ growth of CdS quantum dots on g-C$_3$N$_4$ nanosheets for highly; efficient photocatalytic hydrogen generation under visible light;irradiation, Int. J. Hydrogen Energ. 38 (2013) 1258–1266.

[26] W. Chen, T.Y. Liu, T. Huang, X.H. Liu, J.W. Zhu, G.R. Duan, X.J. Yang, In situ fabrication of novel Z-scheme Bi$_2$WO$_6$ quantum dots/g-C$_3$N$_4$ ultrathin nanosheets heterostructures with improved photocatalytic activity, Appl. Surf. Sci. 355 (2015) 379–387.

[27] K. Wang, G. Zhang, J. Li, Y. Li, X. Wu, 0D/2D Z-Scheme Heterojunctions of bismuth tantalate quantum dots/ultrathin g-C$_3$N$_4$ nanosheets for highly efficient visible light photocatalytic degradation of antibiotics, ACS Appl. Mater. Interfaces 9 (2017) 43704–43715.

[28] L. Tang, C.T. Jia, Y.C. Xue, L. Li, A.Q. Wang, G. Xu, N. Liu, M.H. Wu, Fabrication of compressible and recyclable macroscopic g-C$_3$N$_4$/GO aerogel hybrids for visible-light harvesting: a promising strategy for water remediation, Appl. Catal. B 219 (2017) 241–248.

[29] L. Qu, N. Wang, H. Xu, W. Wang, Y. Liu, L. Kuo, T.P. Yadav, J. Wu, J. Joyner, Y. Song, Gold nanoparticles and g-C$_3$N$_4$-intercalated graphene oxide membrane for recyclable surface enhanced raman scattering, Adv. Funct. Mater. 27 (2017) 1701714.

[30] P. Yang, H. Ou, Y. Fang, X. Wang, A facile steam reforming strategy to delaminate

[31] Y. Xu, H. Bai, G. Lu, C. Li, G. Shi, Flexible graphene films via the filtration of water-soluble noncovalent functionalized graphene sheets, J. Am. Chem. Soc. 130 (2008) 5856–5857.

[32] M.Y. Ye, Z.H. Zhao, Z.F. Hu, L.Q. Liu, H.M. Ji, Z.R. Shen, T.Y. Ma, 0D/2D heterojunctions of vanadate quantum dots/graphitic carbon nitride nanosheets for enhanced visible-light-driven photocatalysis, Angew. Chem. Int. Ed. 129 (2017) 8407–8411.

[33] L. Qiu, J.Z. Liu, S.L. Chang, Y. Wu, D. Li, Biomimetic superelastic graphene-based cellular monoliths, Nat. Commun. 3 (2012) 1241.

[34] M. Tahir, C. Cao, N. Mahmood, F.K. Butt, A. Mahmood, F. Idrees, S. Hussain, M. Tanveer, Z. Ali, I. Aslam, Multifunctional g-C$_3$N$_4$ nanofibers: a template-free fabrication and enhanced optical, electrochemical, and photocatalyst properties, ACS Appl. Mater. Interfaces 6 (2014) 1258–1265.

[35] L. Liu, S.H. Chung, A. Manthiram, Three-dimensional self-assembled SnS$_2$-nanodots@graphene hybrid aerogel as an efficient polysulfide reservoir for high-performance lithium-sulfur batteries, J. Mater. Chem. A Mater. Energy Sustain. 6 (2018) 7659–7667.

[36] P. Xia, B. Zhu, B. Cheng, J. Yu, J. Xu, 2D/2D g-C$_3$N$_4$/MnO$_2$ nanocomposite as a direct Z-scheme photocatalyst for enhanced photocatalytic activity, ACS Sustain. Chem. Eng. 6 (2018) 965–973.

[37] H. Li, H. Li, S. Wu, C. Liao, Z. Zhou, X. Liu, A.B. Djurišić, M. Xie, C. Tang, K. Shih, Facile synthesis, characterization, and electrochemical performance of multi-scale AgVO$_3$ particles, J. Alloys Compd. 674 (2016) 56–62.

[38] Y. Zheng, L. Lin, X. Ye, F. Guo, X. Wang, Helical graphitic carbon nitrides with photocatalytic and optical activities, Angew. Chem. Int. Ed. 53 (2014) 11926–11930.

[39] J. Hu, D. Chen, N. Li, Q. Xu, H. Li, J. He, J. Lu, 3D aerogel of graphitic carbon nitride modified with perylene imide and graphene oxide for highly efficient nitric oxide removal under visible light, Small 14 (2018) 1800416.

[40] H. Wu, D. Chen, N. Li, Q. Xu, H. Li, J. He, J. Lu, Hollow porous carbon nitride immobilized on carbonized nanofibers for highly efficient visible light photocatalytic removal of NO, Nanoscale 8 (2016) 12066–12072.

[41] Z. Wang, Y. Huang, W. Ho, J. Cao, Z. Shen, S.C. Lee, Fabrication of Bi$_2$O$_2$CO$_3$/g-C$_3$N$_4$ heterojunctions for efficiently photocatalytic NO in air removal: In-situ self-sacrificial synthesis, characterizations and mechanistic study, Appl. Catal. B 199 (2016) 123–133.

[42] Z. Ai, W. Ho, S. Lee, Efficient visible light photocatalytic removal of NO with BiOBr-graphene nanocomposites, J. Phys. Chem. B 115 (2011) 25330–25337.

[43] Y. Huang, Y. Gao, Q. Zhang, Y. Zhang, J.J. Cao, W. Ho, S.C. Lee, Biocompatible FeOOH-Carbon quantum dots nanocomposites for gaseous NOx removal under visible light: improved charge separation and high selectivity, J. Hazard. Mater. 354 (2018) 54–62.

[44] Y. Lu, Y. Huang, J. Cao, W.K. Ho, Q. Zhang, D. Zhu, S.C. Lee, Insight into the photocatalytic removal of NO in air over nanocrystalline Bi$_2$Sn$_2$O$_7$ under simulated solar light, Ind. Eng. Chem. Res. 40 (2016) 10609–10617.

[45] X. Li, D. Chen, N. Li, Q. Xu, H. Li, J. He, J. Lu, AgBr-loaded hollow porous carbon nitride with ultrahigh activity as visible light photocatalysts for water remediation, Appl. Catal. B 229 (2018) 155–162.

[46] Y. Huang, D. Zhu, Q. Zhang, Y. Zhang, J.J. Cao, Z. Shen, W. Ho, S.C. Lee, Synthesis of a Bi$_2$O$_2$CO$_3$/ZnFe$_2$O$_4$ heterojunction with enhanced photocatalytic activity for visible light irradiation-induced NO removal, Appl. Catal. B 234 (2018) 70–78.

[47] W.J. Ong, L.L. Tan, Y.H. Nun, S.T. Yong, S.P. Chai, Graphitic carbon nitride (g-C$_3$N$_4$)-based photocatalysts for artificial photosynthesis and environmental remediation: are we a step closer to achieving sustainability? Chem. Rev. 116 (2016) 7159–7329.

[48] T. Xiong, M. Wen, F. Dong, J. Yu, L. Han, B. Lei, Y. Zhang, X. Tang, Z. Zang, Three dimensional Z-scheme (BiO)$_2$CO$_3$/MoS$_2$ with enhanced visible light photocatalytic NO removal, Appl. Catal. B 199 (2016) 87–95.

[49] F. Dong, Z. Zhao, Y. Sun, Y. Zhang, S. Yan, Z. Wu, An Advanced Semimetal-organic Bi spheres-g-C$_3$N$_4$ nanohybrid with SPR-enhanced visible-light photocatalytic performance for NO purification, Environ. Sci. Technol. 49 (2015) 12432–12440.

[50] Y. Lu, Y. Huang, Y. Zhang, J.J. Cao, H. Li, C. Bian, S.C. Lee, Oxygen vacancy engineering of Bi$_2$O$_3$/Bi$_2$O$_2$CO$_3$ heterojunctions: implications of the interfacial charge transfer, NO adsorption and removal, Appl. Catal. B 231 (2018) 357–367.

[51] Y. Huang, Y. Liang, Y. Rao, D. Zhu, J.J. Cao, Z. Shen, W. Ho, S.C. Lee, Environment-friendly carbon quantum dots/ZnFe$_2$O$_4$ photocatalysts: characterization, biocompatibility, and mechanisms for NO removal, Environ. Sci. Technol. 51 (2017) 2924–2933.

[52] P. Chen, H. Wang, H. Liu, Z. Ni, J. Li, Y. Zhou, F. Dong, Directional electron delivery and enhanced reactants activation enable efficient photocatalytic air purification on amorphous carbon nitride co-functionalized with O/La, Appl. Catal. B 242 (2019) 19–30.

[53] X. Li, W. Zhang, J. Li, G. Jiang, Y. Zhou, S.C. Lee, F. Dong, Transformation pathway and toxic intermediates inhibition of photocatalytic NO removal on designed Bi metal@defective Bi$_2$O$_2$SiO$_3$, Appl. Catal. B 241 (2019) 187–195.

[54] W. Cui, J. Li, Y. Sun, H. Wang, G. Jiang, S.C. Lee, F. Dong, Enhancing ROS generation and suppressing toxic intermediate production in photocatalytic NO oxidation on O/Ba co-functionalized amorphous carbon nitride, Appl. Catal. B 237 (2018) 938–946.